Nanoscale Science – Semiconductor Nanostructures

1. Basic concepts

1.1 Optical properties of semiconductors

A photon of energy hν greater than the bandgap energy E_g can be absorbed in a semiconductor, resulting in the excitation of an electron from the valence band to the conduction band. The average energy of electrons in the conduction band is $3/2 \cdot k_B T$ above E_C. If the photon energy is much larger than E_g, then the excited electron is not near E_C and has to lose the extra energy ($h\nu$ - E_g) to reach thermal equilibrium. The excess energy is lost to lattice vibrations as heat as the electron is scattered from one atomic vibration to another. This process is called thermalization. If, on the other hand, the photon energy hν is less than E_g, the photon will not be absorbed, and the semiconductor will be transparent to wavelengths longer than hc/E_g provided that there are no energy states in the band gap. Suppose that I_0 is the intensity of a beam of photons incident on a semiconductor material. Thus, I_0 is the energy incident per unit area per unit time. If Γ_{ph} is the photon flux, then

$$I_0 = h\nu\,\Gamma_{ph}$$

The optical absorption depends on the thickness of the semiconductor. If $I(x)$ is the light intensity at position x and δI is the change in the light intensity in the small elemental volume of thickness δx at x due to phonon absorption, then δI will depend on the number of phonons arriving at this volume $I(x)$ and the thickness δx:

$$\delta I = -\alpha\, I\, \delta x$$

where α is the **absorption coefficient** of the semiconductor, whose magnitude depends on the photon energy. Integration of the above equation for illumination with constant wavelength light yields the **Beer-Lambert law**, which reveals that the transmitted intensity decreases exponentially with the thickness:

$$I(x) = I_0 \exp(-\alpha x)$$

The distance of $x = 1/\alpha$, over which the light intensity falls to a value of I_0/e, is called the **penetration depth** δ.
The absorption coefficient depends on the photo absorption processes occurring in the semiconductor. In the case of **band-to-band (interband) absorption**, α increases rapidly with the photon energy hν above E_g. The general trend of the α vs. $h\nu$ behaviour follows the corresponding density of states $g(E)$, which increases from the band edges and usually exhibits peaks and troughs. Generally α increases with the photon energy greater than E_g because more energetic photons can excite electrons from populated regions of the valence band to available states deep in the conduction band.

Optical absorption in semiconductors can be understood in terms of the behaviour of the electron energy (E) with the electron momentum ($\hbar k$) in the crystal, called the crystal momentum. In a **direct bandgap** semiconductor such as III-V semiconductors (*e.g.*, GaAs, InAs, InP, GaP) and in many of their alloys (*e.g.*, InGaAs, GaAsSb) the photon absorption process requires no assistance from lattice vibrations. Upon photon absorption, the electron is excited directly from the valence into the conduction band without a change in its k-vector. This process corresponds to a vertical transition in the E vs. $\hbar k$ diagram. The absorption coefficient of direct bandgap materials rises sharply with decreasing wavelength from λ_g. In **indirect bandgap** semiconductors such as Si or Ge, the photon absorption requires the absorption or emission of a phonon. If K is the wavevector of a lattice wave, then $\hbar K$ represents the associated phonon momentum. When an electron in the valence band is excited to the conduction band, there is a change in its momentum in the crystal, and this momentum change cannot be supplied by the very small momentum of the incident photon. Thus, the momentum difference must be balanced by a phonon momentum. The absorption process is said to be indirect as it depends on lattice vibrations which in turn depend on the temperature. Since the interaction of a photon with a valence electron needs a third body, a lattice vibration, the probability of photon absorption is lower than in a direct transition. Furthermore, the cut-off wavelength is not as sharp as in the latter case.

Optical absorption in crystalline semiconductors can create an **exciton**, which is an electron and hole pair excited by a photon and bound together through their attractive Coulomb interaction. This means that the absorbed optical energy remains held within the solid for the lifetime of the exciton. There are two types of excitons that can be formed in non-metallic solids, namely **Wannier-Mott excitons** and Frenkel excitons. While Frenkel excitons occur in organic crystals, the concept of Wannier-Mott excitons is valid for inorganic semiconductors, because in these materials the large overlap of interatomic electronic wavefunctions enables the electrons and holes to be far apart but bound in an excitonic state.

In Wannier-Mott excitons, the Coulomb interaction between the hole and the electron can be viewed as an effective hydrogen atom with the hole establishing the coordinate reference frame about which the reduced mass electron moves. If the effective mass of the isolated electron and hole are m_e^* and m_h^*, respectively, their reduced mass μ_x is given by:

$$\frac{1}{\mu_x} = \frac{1}{m_e^*} + \frac{1}{m_h^*}$$

The energy of a Wannier-Mott exciton is given by

$$E_x = E_g + \frac{\hbar^2 K^2}{2M} - E_n$$

where $\hbar K$ is the linear momentum, $M = m_e^* + m_h^*$ is the effective mass associated with the centre of mass of the exciton, and E_n is the exciton binding energy given by

$$E_n = \frac{\mu_x e^4 \kappa^2}{2\hbar^2 \varepsilon^2} \frac{1}{n^2}$$

where e is the electronic charge, $\kappa = \frac{1}{4\pi\varepsilon_0}$, and n is the principal quantum number associated with the internal excitonic states n = 1(s), 2(p),… It follows that the excitonic states are formed within the band gap below the conduction band edge. However, as the exciton binding energy is very small (a few meV in bulk Si and Ge), exciton absorption peaks can only be observed at low temperatures. Extrapolating from the hydrogen atom model, the extension of the excitonic wavefunction can be found from an **effective Bohr radius** $a_{exciton}$ given in terms of the Bohr radius a_B as

$$a_{exciton} = a_B \left(\frac{\varepsilon}{\mu_x} \right)$$

with ε as the dielectric constant of the semiconductor, and a_B given as

$$a_B = \frac{4\pi\varepsilon_0 \hbar^2}{m_e e^2} = 5.29 \cdot 10^{-11} \text{m}$$

As an example, the exciton radius in GaAs is ~14 nm, corresponding to approximately 21 lattice constants (in other words, the spherical volume of the exciton radius contains ~9000 unit cells). Since exciton states lie below the conduction band edge, **excitonic absorption** is observed below this edge. The difference in energy in the bandgap and the excitonic absorption corresponds to the exciton binding energy.

The interband optical absorption process leads to the production of free carriers in the conduction and valence bands. These free carriers, constituting excited states, have relatively short lifetimes and tend to recombine with the emission of photons in a process called radiative recombination. This process is called **photoluminescence**, in case that the excitation is caused by a light beam producing the free electron-hole population. One can make the same distinctions in radiative recombinations as in optical absorption according to the band structure of the material. A radiative recombination transition can be direct or indirect depending on whether or not it is phonon-assisted. In a direct gap material, radiative recombination occurs without phonon participation, and the process is direct. The frequency of the emitted light corresponds to the direct (optical) gap energy. In an indirect gap material, the excited carriers thermalize in the lowest conduction band minimum, which typically is at $k \neq 0$. Thus, the radiative recombination process is accompanied by phonon emission to account for the momentum change of the carrier. Because momentum must be conserved in a band-to-band electron-hole recombination, and since the momentum of the emitted phonon is nearly zero, the sum of the recombining carrier momenta must be matched by the momentum of the phonon participating in the process.

The photon absorption results in an excess electron concentration Δn, equal to the excess hole concentration Δp. The time dependence of the excess carrier concentration is governed by the rate equation

$$\frac{d\Delta n}{dt} = -\frac{\Delta n}{\tau}$$

where τ is the **carrier lifetime**. The carrier lifetime represents the average time a carrier spends in a given band before recombination. It should be clearly distinguished from the relaxation time or characteristic time in transport, corresponding to intraband scattering of a carrier. The relaxation time is the time between two collisions in which the carrier changes state, and is generally much smaller than the lifetime. It is furthermore convenient to introduce the **recombination rate** R defined by

$$R = -\frac{d\Delta n}{dt} = \frac{\Delta n}{\tau}$$

The thermalization of carriers is not exclusively radiative. Non-radiative recombination may occur through the successive emission of phonons, producing heat, or through Auger processes wherein the recombination energy is transferred to a third carrier, which is elevated into the conduction band if it is an electron, or lowered into the valence band if it is a hole. Let the radiative recombination rate in a material per unit volume be R_r and the non-radiative be R_{nr}. The **internal quantum efficiency** η_i of photoluminescence is then given by

$$\eta_i = \frac{R_r}{R_r + R_{nr}}$$

1.2 Quantum confinement

1.2.1 Three-dimensional systems

A three-dimensional bulk material can be modelled as an infinite crystal along all three dimensions x, y, z (figure 1). The periodic boundary conditions yield standing waves as solutions of the Schrödinger equation for free electrons. The associated wavenumbers (k_x, k_y, k_z) are periodically distributed in the reciprocal k-space. Each state in k-space can be only occupied by two electrons ($m_s = \pm ½$). In a large solid, the spacing $\Delta k_{x,y,z}$ between individual electron states is very small and therefore the k-space is quasi-continuously filled with states. A sphere with radius k_F includes all states with $k = (k_x^2 + k_y^2 + k_z^2)^{1/2} < k_F$. In the ground state, at 0 K, all states with $k < k_F$ are occupied with two electrons, while all other states are empty. The energy of free electrons in bulk solids scales with the square of the wavenumber, corresponding to a parabolic dependence on k, with a very small distance between adjacent states.

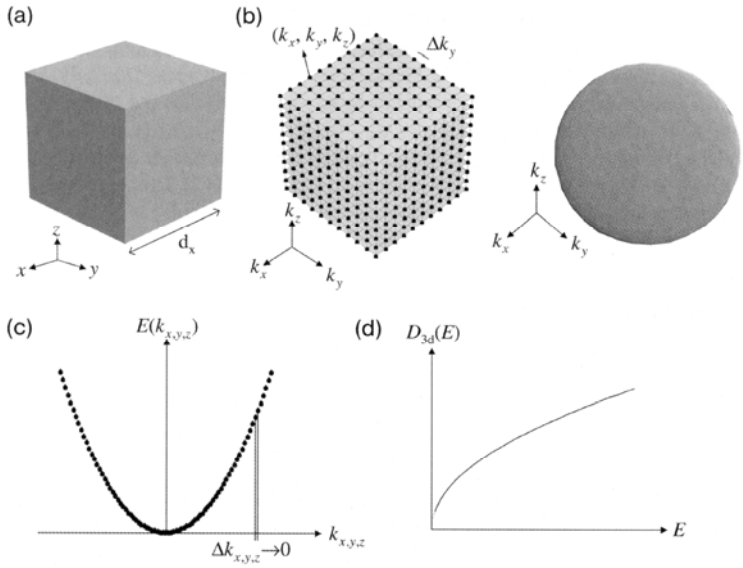

Figure 1: Electrons in a three-dimensional bulk solid.

Since the *k*-space is homogeneously filled with states, the number of states within a certain volume scales with k^3. Thus, the density of states as a function of *k* is given as

$$D_{3D}(k) = \frac{\mathrm{d}N(k)}{\mathrm{d}k} \propto k^2$$

On this basis, the density of states as a function of energy is obtained to

$$D_{3D}(E) = \frac{\mathrm{d}N(E)}{\mathrm{d}E} = \frac{\mathrm{d}N(k)}{\mathrm{d}k}\frac{\mathrm{d}k}{\mathrm{d}E} \propto E \cdot \frac{1}{\sqrt{E}} \propto \sqrt{E}$$

1.2.2 One-dimensional systems

The electronic states of a one-dimensional solid (figure 2) can be obtained in an analogous manner as described for the three-dimensional case. The electrons are free move in the x-direction, and the allowed (k_x, k_y, k_z) states can be visualized as lines parallel to the k_x-axis in the three-dimensional *k*-space. Within each line, the distribution of states is quasi-continuous. The arrangement of the individual lines is discrete, since only certain discrete k_y and k_z states are allowed. Thus, along the k_x-axis the energy band $E(k_x, k_y, k_z)$ is quasi-continuous, but along the k_y- and k_z-axis, only certain energies exist. In a one-dimensional system, the number of states is proportional to $k = k_x$, and hence the density of states as a function of *k* is given as

$$D_{1D}(k) = \frac{\mathrm{d}N(k)}{\mathrm{d}k} \propto 1$$

From this equation, the density of states as a function of energy is obtained to

$$D_{1D}(E) = \frac{\mathrm{d}N(E)}{\mathrm{d}E} = \frac{\mathrm{d}N(k)}{\mathrm{d}k}\frac{\mathrm{d}k}{\mathrm{d}E} \propto 1 \cdot \frac{1}{\sqrt{E}} \propto \frac{1}{\sqrt{E}}$$

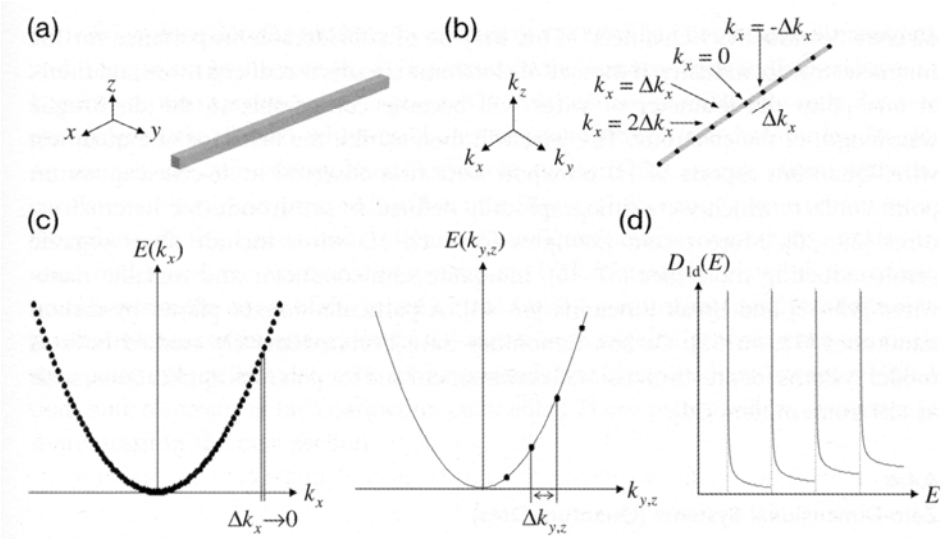

Figure 2: Electrons in a one-dimensional solid.

The $E^{-½}$ dependence manifests itself in hyperbolic tails, which represent singularities near the band edges. Each of the hyperbolas contains a continuous distribution of k_x states, but only one discrete k_y and k_z state.

1.2.3 Zero-dimensional systems

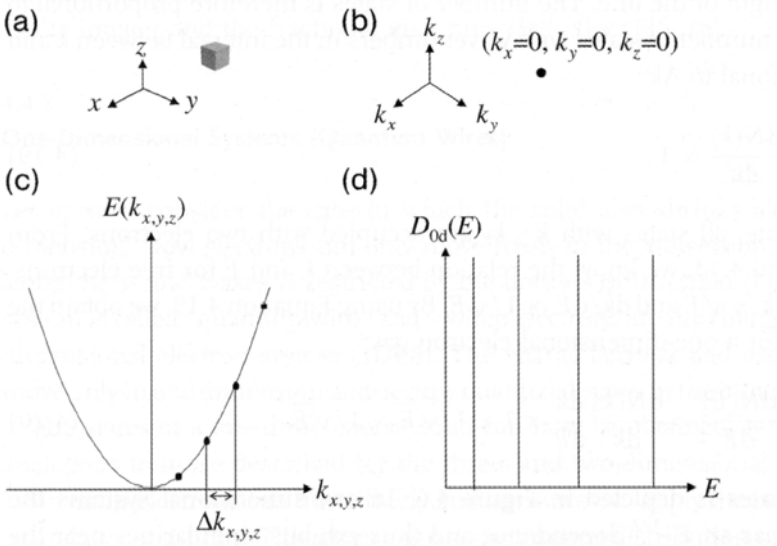

Figure 3: Electrons in a zero-dimensional solid.

When the charge carriers are confined in all three dimensions, the system is called a "quantum dot" (QD). In a QD, there exist only discrete (k_x, k_y, k_z) states (figure 3). Each individual state can be represented by a point in the *k*-space. As a consequence, only discrete energy levels are allowed, *i.e.*, the energy bands converge to atom-like energy states, which leads to the emergence of delta peaks in the electronic density of states.

2. Zero-dimensional nanostructures: Semiconductor nanocrystals (quantum dots)

2.1 Synthesis of surfactant-stabilized semiconductor nanocrystals

2.1.1 Particle nucleation and growth

As demonstrated in classical studies by LaMer *et al.*, the synthesis of monodisperse colloids via homogeneous nucleation requires a temporal separation of nucleation and growth of the seeds [1]. The LaMer plot (figure 4) is very useful to illustrate the separation of nucleation and growth by means of a nucleation burst. Initially the concentration of monomers, i.e. the minimum subunits of the crystal, constantly increases by addition from exterior or by in situ generation within the reaction medium. It should be noted that in stage I no nucleation occurs even in supersaturated solution (S > 1), due to the extremely high energy barrier for spontaneous homogeneous nucleation. The latter is overcome in stage II for a yet higher degree of supersaturation ($S > S_c$), where nucleation and formation of stable nuclei take place. As the rate of monomer consumption induced by the nucleation and growth processes exceeds the rate of monomer supply, the monomer concentration and hence the supersaturation decreases below S_c, the level at which the nucleation rate becomes zero. In the following stage III, the particle growth continues under further monomer consumption as long as the system is in the supersaturated regime.

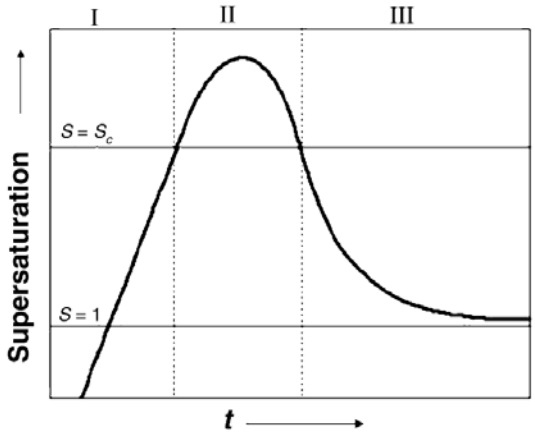

Figure 4: LaMer plot depicting the degree of supersaturation as a function of reaction time.

Experimentally, the separation of nucleation and growth can be achieved by rapid injection of the reagents into the hot solvent, which raises the precursor concentration in the reaction flask above the nucleation threshold ("hot-injection method"). The hot-

injection leads to an instantaneous nucleation, which is quickly quenched by the fast cooling of the reaction mixture (the solution to be injected is at room temperature) and by the decreased supersaturation after the nucleation burst. Another possibility relies on attaining the degree of supersaturation necessary for homogeneous nucleation via the in situ formation of reactive species upon supply of thermal energy ("heating-up method"). An increasing number of examples of semiconductor NCs are prepared by this approach. In an ideal case, all crystallization nuclei are created at the same time and undergo identical growth. During the growth stage it is possible to carry out subsequent injections of precursors in order to increase the mean particle size without deterioration of the narrow size distribution as long as the concentration corresponding to the critical supersaturation S_c is not exceeded. Crystal growth from solution is in many cases followed by a second distinct growth process, which is referred to as Ostwald ripening. It consists of the dissolution of the smallest particles because of their high surface energy and subsequent re-deposition of the dissolved matter onto the bigger ones. Thereby the total number of NCs decreases, whereas their mean size increases. As shown in early studies, Ostwald ripening can lead to reduced size dispersions of micron-sized colloids. In the case of nanometer-sized particles, however, Ostwald ripening generally yields size dispersions of the order of 15–20%, and therefore the reaction should be stopped before this stage. From a thermodynamic point of view, if diffusion is the rate-limiting step, the size-dependent growth rate can be expressed by means of the Gibbs-Thompson equation:

$$L(r) = L_{bulk} \exp(2\gamma V_m / rRT)$$

where $L(r)$ and L_{bulk} are the solubilities of a NC with radius r and of the bulk solid, respectively, γ is the specific surface energy, V_m the molar volume of the solid, R the gas constant, and T the temperature [2]. The validity of the Gibbs-Thompson equation and the focusing of size distributions during the diffusion-controlled NC growth are experimentally well-documented. Using the hot-injection or heating-up synthesis methods, it is possible to obtain samples with 5 - 10% standard deviation from the mean size without post-preparative size fractionation.

2.1.2 Chemical synthesis of monodisperse semiconductor nanocrystals

Initially developed procedures for semiconductor NC synthesis employed homogenous aqueous solutions containing appropriate reagents and surfactant-type or polymer-type stabilizers. The latter bind to the NC surface and stabilize the particles by steric hindrance and/or electrostatic repulsion in the case of charged stabilizers. In parallel to this monophase synthesis, a bi-phase technique has been developed, which is based on the arrested precipitation of NCs within inverse micelles. Here nanometer-sized water droplets (dispersed phase) are stabilized in an organic solvent (continuous phase) by an amphiphilic surfactant. They serve as nano-reactors for the NC growth and prevent at the same time from particle agglomeration. Both methods provide relatively simple experimental approaches using standard reagents as well as room temperature reactions and were of great importance for the development of NC synthesis. Furthermore, for some materials (e.g. mercury chalcogenides) the aqueous synthetic technique is the only

successful preparation method reported today. On the other hand, the samples prepared by these synthetic routes usually exhibit size dispersions at least of the order of 15% and therefore fastidious procedures of NCs separation into "sharp" fractions have to be applied in order to obtain monodisperse samples. The introduction of a high temperature preparation method using organic solvents in 1993 constituted an important step towards the fabrication of monodisperse CdS, CdSe and CdTe NCs [3]. It involves the decomposition of molecular precursors, *i.e.*, molecules that deliver the monomers of the nanoparticles, at relatively high temperatures (figure 5). Precursors are injected swiftly into a hot solvent. By this, the monomers, i.e. the atomic species that constitute the nanocrystal, are freed rapidly leading to a high oversaturation of monomers.

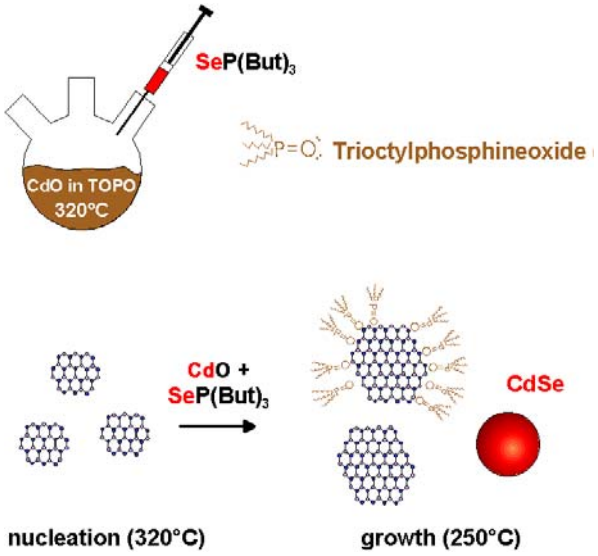

Figure 5: Synthesis of capped CdSe nanocrystals from a selenium precursor and cadmium oxide (CdO). The added TOPO acts as a surface-stabilizing surfactant.

The use of organic solvents has the advantage that one can tune the reaction temperature over a wide range. Temperature and composition of the solvent exert strong influence on the growth kinetics and on the shape of the nanocrystals. Also, through the reaction environment the crystalline phase of the material can be influenced. For instance, CdTe nanocrystals being synthesized at high temperature in organic solvents generally grow in the hexagonal wurtzite phase. However, by a careful control of the reaction conditions they can also be grown in the cubic zincblende phase. As surfactants, tri-n-octylphosphine oxide (TOPO) and tri-n-octylphosphine (TOP) are frequently used. Other types of ligands are organic amines and carboxylic acids. The reaction is usually carried out under an inert atmosphere, as some of the reactants may be pyrophoric and also some types of nanocrystals may be sensitive to air. After loading the flask with the organic solvent and surfactant molecules, these organic molecules are molten from powder state to a liquid and the flask is evacuated and kept under vacuum at ca. 130 - 180°C for 10 - 20 min to remove volatile impurities. This step is crucial for most syntheses. Before starting the actual reaction the flask is flushed with an inert gas. For the growth of II/VI semiconductor NCs the elemental chalcogens are introduced into the reaction as a complex with TOP. In the early syntheses of CdE (E = S, Se or Te) nanocrystals dimethyl

cadmium has been used as precursor. This liquid compound along with Se/TOP is injected into the reaction solution to initiate the growth of CdSe nanocrystals, but unfortunately it is unstable, highly toxic and pyrophoric. In the modern syntheses this compound is usually replaced by CdO. At a temperature of ~300°C the Cd ions bind to the surfactants, whereupon a color change of the solution from dark red to translucent occurs. In this reaction scheme only the chalcogen complex is injected and the nucleation sets in shortly after the injection.
II-VI semiconductor bulk materials have two crystalline structures, cubic (zincblende) and hexagonal (wurtzite) types. For the bulk materials, CdS has highly stable hexagonal phase from room temperature to the melting point (1750°C), while bulk ZnS has the cubic structure. Because the difference in the crystalline structure of the bulk semiconductor materials leads to considerable change in the effective masses of the carriers in their electronic bands, the crystalline structure of semiconductor NCs plays a dominant role in determining their photochemical, photocatalytic, and photophysical properties. Phase transformation of semiconductor NCs can be achieved under high temperature and pressure, although these extreme conditions often cause unexpected structural deformations, such as the growth of the NCs and change of their chemical composition. Control of the crystalline structure has furthermore been achieved at ambient temperature and pressure through the chemical modification of the ZnS NC surface with different organic molecules. Thiols, for example, are capable to chemically bind to the surface of ZnS nanocrystallites, and change the hexagonal phase of the NCs to the cubic.

2.1.3 Shape control of semiconductor nanocrystals

There has been inspiring progress in the synthesis of semiconductor NCs with various shapes, ranging from rods, to teardrops, pyramids and structured pyramids, tetrapods, and rather complex hyperbranched systems. The deciding factor for shape control is the specific interactions between different ligand systems and various NC facets. Small crystals have substantial numbers of surface atoms compared to internal atoms, so the energy contribution of surfaces and facets to the total energy of a nanocrystal is dominant. Thus, simple crystals evolve to minimize the total of the product of surface area times the surface energy for each facet. Importantly, there are two primary factors that contribute to the total energy of the system by a nanocrystalline colloid at equilibrium. One is the chemical potential associated with each crystal face in isolation, and the other is the surface tension of each of these facets. Realizing that the synthesis of NCs involves annealing to attain an equilibrium shape, which is close to spherical for a homogeneous passivating ligand, provides a clue about how that shape can be altered (figure 6). The system free energy F at equilibrium satisfies

$$dF \approx 0 \approx -(p'' - p')dV'' + \sum_{\alpha} \gamma_{\alpha} dA_{\alpha}$$

where (p''- p') is the excess pressure of the solid phase, V'' is the volume of the solid phase, γ_a is the surface tension of the crystal face labeled α, and A_α is its surface area. The equation says that the work done in adding material to any facet of the nanocrystal is

compensated for by a change in surface energy. Therefore, to change the shape of a nanocrystal from that typically assumed at equilibrium conditions we must modify the surface tension of crystal faces. This can be done by changing the ligands bound to these crystal faces, and, indeed, the concept of facet-selective ligand adsorption is central to the shape control of NCs [4].

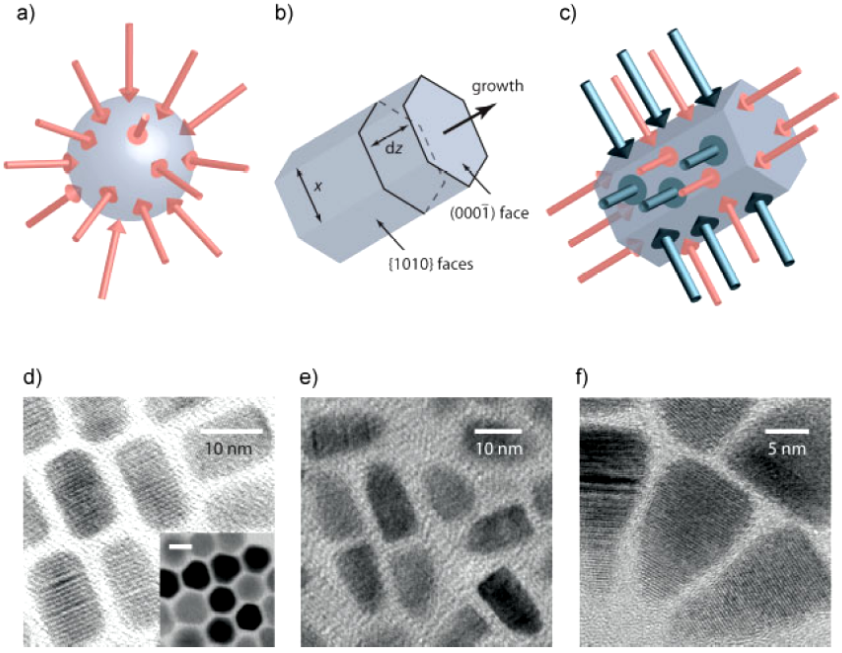

Figure 6: Shape control of semiconductor NCs. a) An ideal spherical nanocrystal has a balance of surface tension provided by uniform ligand coverage. b) Diagram showing a hexagonal NC growing in length by a small amount *dz* along the c-axis. c) The resulting rod-shape must be stabilized by non-uniform ligand coverage so that the surface tension is lowered on the sides relative to the ends. d)-f) TEM images of CdSe rods, bullets, and pyramids, demonstrating that growth can be directed in a unique direction along the c-axis by changing the ligand composition as a function of growth stage.

The meaning of above equation can be grasped by considering the simple case of elongating a short Wurtzite nanorod "seed". Starting from a model hexagonal prism, let's imagine increasing only the length along the c-axis by a small amount *dz*. Assuming the truncation is unchanged and only the length of the {1010} faces are increased during this growth, then we find that the effect of this elongation is to increase the surface energy by $6\gamma_{1010}xdz$ and the volume by $dV'' = \sqrt[3]{3x^2 dz/2}$. This yields an excess pressure in the solid phase of

$$(p'' - p') = 4\gamma_{1010}/(x\sqrt{3})$$

To stabilize the nanorod, that excess pressure must be compensated for by a change in γ_{1010}. The surface tension of the {1010} faces must be decreased. As is well known in surface chemistry, surfactants lower surface tension, so they are employed in NC synthesis to modify selectively the γ_α. Conceptually, the process is analogous to thinking about how to elongate a drop of liquid on a surface, which is simply to apply uniform

pressure along the sides of the drop (‘‘squash’’ it). Similarly, the ligands ‘‘push’’ on the surface of a NC to stabilize its shape by moderating the surface tension of distinct crystal faces to differing extents.
Shape evolution is often thought about in terms of growth; the quasi-equilibrium structure at any time therefore depends on the history of the relative growth rates of different faces. Hence slower growing faces become more prominent than fast growing ones. In a microscopic picture of the growth process, the ligands must desorb from a site before the crystal can grow at that site. Therefore, strongly adsorbed (tightly bound) ligands retard growth, while more labile ligands enable vectorial growth on crystal faces to which they are adsorbed. This view of shape control is termed ‘‘kinetic growth’’, and it leads to the same conclusions for equilibrium conditions as described above. For example, if one end of a CdSe nanorod has a particularly high surface tension under certain solvent–ligand conditions, then it is desirable to eliminate this face. That is achieved by ensuring growth in the direction normal to that face is faster than in any other direction. The fastest growing face, which in the case of Wurtzite CdSe is the anion-rich (0001) face, is eliminated and replaced by steps, or facets. The result is seen in the ‘bullet’ and pyramidal CdSe NCs, where the basal plane therefore should be the (0001) face. These NCs were grown by sequentially altering the balance of ligands in the growth solution using a multiple injection strategy [5]. That process has been used also, for example, to grow PbSe selectively onto one end only of a CdSe rod.

Another application example of the growth control strategies outlined above is the synthesis of tetrapod-shaped semiconductor NCs. Tetrapods made of CdTe (figure 7) can be obtained by controlling the relative stability and growth of two different crystal phases [6].

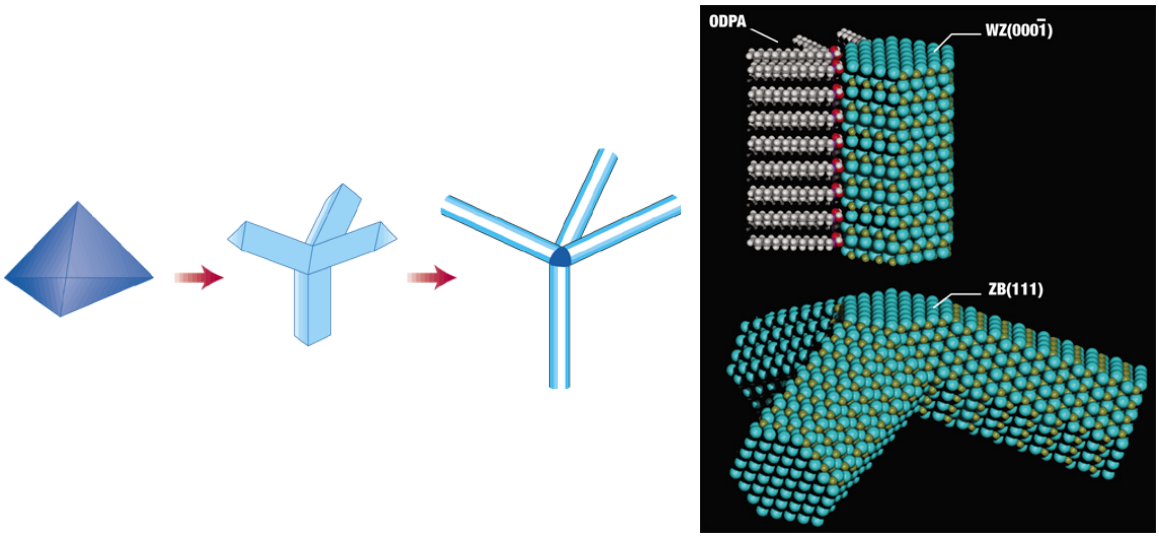

Figure 7: Schematic representation of the growth of tetrapod-shaped nanocrystals from a nanocrystal core (*left*). The surfactant ODPA (an organic phosphonic acid) is able to selectively stabilize non-polar lateral facets of CdTe nanocrystals in the zincblende structure (*right*).

In CdTe and other tetrahedrally bonded compound semiconductors, the ±{111} facets of the cubic (zincblende) structure are atomically identical to the ±(0001) facets of the hexagonal (wurtzite) structure. As a consequence, the cubic and hexagonal crystal phases are often sufficiently close in energy such that both can be accessed by simply varying the reaction conditions. A key parameter for achieving tetrapod growth is the energy difference between the wurtzite and the zincblende structures, which determines the temperature range in which one structure can be preferred during nucleation and the other during growth. In case of very ionic or very covalent semiconductors, this difference can exceed 10meV per atom, rendering it impractical to switch between the two growth modes during a reaction. By comparison, the energy difference is only a few meV per atom in CdS, CdSe and ZnS, making it difficult to isolate controllably the growth of one phase at a time. CdTe represents an intermediate case, for which the energy difference between the two crystal structures is large enough that, even at the elevated temperatures preferred for high-quality wurtzite growth, nucleation can occur selectively in the zincblende structure. In CdTe, wurtzite growth is favored by using higher temperatures in the presence of an appropriate surfactant (*e.g.*, an alkyl chain phosphonic acid). These molecules are able to stabilize selectively the non-polar lateral facets of CdTe nanocrystals, which have no equivalent in the cubic structure. Hence, following initial nucleation of cubic nanocrystals with tetrahedral morphology and four (111) crystal facets, four hexagonal arms can be selectively grown from the tetrahedral cubic nuclei. The rate of axial elongation versus radial thickening of the arms can be independently controlled through variations in the reactant and surfactant concentrations. It is furthermore remarkable that the lengths of the arms of individual tetrapods are the same to within a few percent, suggesting that the four facets of the initial cubic crystallites have nearly identical reactivity when the hexagonal phase starts to grow. Moreover, the length and diameter of the tetrapod structures can be varied independently through well-defined changes in the Cd/Te and Cd/surfactant ratios, as is consistent with kinetically controlled growth of the arms.

2.2 Energy states and optical transitions in semiconductor nanocrystals

2.2.1 Size dependence of optical absorption

Semiconductor nanocrystals, or quantum dots (QDs), can be considered as an intermediate species between atoms or molecules on the one hand and bulk material on the other hand. The boundaries between molecular, NC, and bulk regimes are not well defined and are strongly material dependent. Bulk crystalline structure is preserved in NCs, but due to quantum confinement NCs have molecular-like discrete energy spectra, which exhibit strong size dependence. This provides an opportunity for a wide-range tailoring of their electronic and optical properties. For example, the energy gap in CdSe NCs can be tuned from 1.8 eV (red) to ~3 eV (UV) by changing the NC diameter from 11.5 to 1.2 nm (figure 8). As size is reduced, the electronic excitations shift to higher energy, and there is concentration of oscillator strength into just a few transitions. Experimentally, the preparation of monodisperse NC samples ($\sigma < 5\%$) has made it

possible to observe, assign, and monitor the size evolution of a series of discrete, excited electronic states [7].

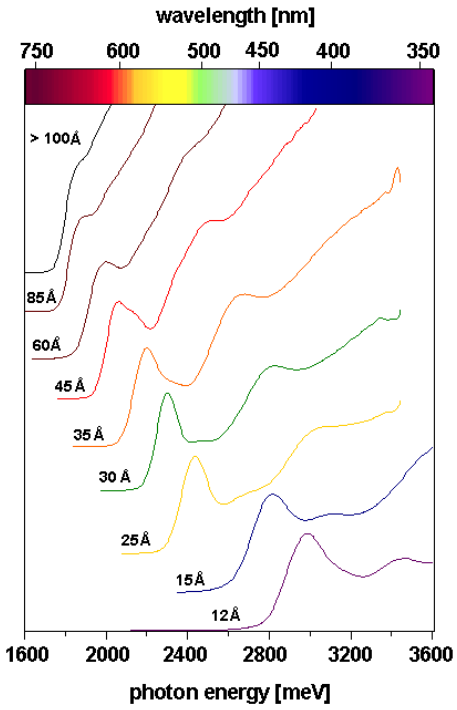

Figure 8: Size-dependence of optical absorption spectra recorded from CdSe nanocrystals with diameters ranging between 1.2 and 8.5 nm.

2.2.2 Simplified electronic structure model

The electronic spectrum of a QD can be derived to first approximation using the particle-in-a-box model. This involves carrier confinement inside an infinite three-dimensional quantum well, whose width d is smaller than the de Broglie wavelength of the carriers. The potential energy is zero everywhere inside the well, but is infinite at its walls. If the shape of the box is cubic, the Schrödinger equation can be solved independently for each of the three translational degrees of freedom, and the overall zero-point energy is simply the sum of the individual zero point energies for each degree of freedom:

$$E_{well,3D(cube)} = 3E_{well,1D} = \frac{3}{8}\frac{h^2}{md^2}$$

If the box is a sphere, the Schrödinger equation can be solved by introducing spherical coordinates and by separating the equation in a radial part and a part containing the angular momentum. The lowest energy level (with angular momentum = 0) is then

$$E_{well,3D(sphere)} = \frac{1}{2}\frac{h^2}{md^2}$$

It can be seen that the zero-point energy of carriers within a sphere of diameter d is larger than for confinement inside a cube with edge length d. This difference arises because such a sphere has a smaller volume [$(\pi/6)d^3$] than the cube (d^3).

The minimum energy E_g(dot) required for creating an electron-hole pair in a QD comprises several contributions. One contribution is the bulk band gap energy E_g(bulk). Another important contribution is the confinement energy for the electron-hole pair, which is approximately given by the zero point energy for the reduced mass μ_x within the potential well:

$$E_{well} = \frac{h^2}{2\mu_{exc} d^2}$$

A third term that has to be included is the Coulomb interaction E_{Coul} between the electron and hole, whose magnitude depends on the extent of dielectric screening inside the material (characterized by the dielectric constant ε):

$$E_{Coul} = -\frac{1.8e^2}{2\pi\varepsilon\varepsilon_0 d}$$

In total, the energy gap energy of a spherical QD is estimated to be

$$E_g(\text{dot}) = E_g(\text{bulk}) + \frac{h^2}{2\mu_{exc} d^2} - \frac{1.8e^2}{2\pi\varepsilon\varepsilon_0 d}$$

While the confinement energy increases with decreasing size as $1/d^2$, the Coulomb energy, which grows only as $1/d$, becomes only a small correction in small QDs of radius $a = d/2$ being much smaller than the Bohr radius of the bulk exciton $a_{exciton} = a_B \varepsilon / \mu_{exc}$. Accordingly, the confinement energy becomes the predominant term, and an electron and a hole can be treated as independent particles. In large QDs with $a >> a_{exciton}$, by contrast, the Coulomb interaction is more important than the confinement energies of the electrons and holes, and the QD energy spectra are determined by quantization of the motion of the exciton center of mass.

2.2.3 Additional effects on electronic structure

The simplified model described above provides a reasonable description of the conduction band in semiconductor QDs. However, because of the complex, multi-subband character of the valence band, one can only explain the valence-band structure by considering confinement-induced mixing between different subbands [8]. In the case of a QD, the valence-band Hamiltonian contains both the crystal-lattice and QD-confinement potentials. For this situation, the true quantum number is the total angular momentum (F) which is a sum of the angular momentum, J, and the orbital momentum

of the hole envelope function (L): $F = J + L$. On this basis, the valence band states are usually denoted as nL_F.

In II-VI semiconductors with diamond, zincblende, and wurtzite lattices, the lowest conduction minimum is formed from s-type orbitals and is twofold degenerate due to electron spin. The valence band formed from p-type wavefunctions is sixfold degenerate. The **spin-orbit (SO) interaction** splits the valence band into a fourfold degenerate band with a total unit-cell angular momentum $J = 3/2$ and a twofold degenerate band with $J = ½$. The energy separation between these bands (Δ_{SO}) is determined by the strength of the spin-orbit interaction. In a semiconductor with wurtzite structure, the $J = 3/2$ band is further split into **light- and heavy-hole subbands** with J projections $Mj = \pm 1/2$ and $\pm 3/2$, respectively. The resulting overall **valence band mixing** is exemplified in figure 9 for a CdSe DQ.

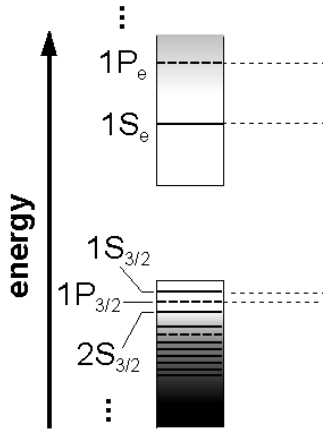

Figure 9: Energy level scheme of a CdSe QD. The electron states are denoted according to their angular momentum J = 0, 1, 2,… as $1S_e$,$1P_e$,$1D_e$, etc., respectively. The valence band levels correspond to single hole states, with the subscript denoting the total angular momentum F = J + L.

2.2.2 Fluorescence properties

Fluorescence of semiconductor nanocrystals is due to the radiative recombination of an excited electron-hole pair. The emission spectrum of a nanocrystal ensemble with narrow size distribution displays a band Stokes-shifted with respect to the excitation band edge (figure 10). Like the optical absorption bands, the fluorescence spectra are blue-shifted as the nanocrystal diameter is reduced. The pronounced Stokes shift is due to the relaxation of excited electrons via acoustic phonon emission from the second or third excited state to the band edge state ($1S_e$), from where radiative recombination occurs.
The ensemble emission spectrum of nanocrystals is very symmetric, in contrast to conventional dyes that suffer from a long IR vibronic tail. However, the full width at half maximum (FWHM) of ~ 30 nm hides the true atomic-like nature of the nanocrystals. The broadening of the ensemble spectrum is due to the size dispersion inherent to the synthesis (inhomogeneous broadening) and spectral diffusion. The latter effect comprises shifts of the main peak position ranging from a fraction of a nanometer to several

nanometers. These spectral jumps are more pronounced at lower temperatures, and likely originate from local charge trapping at the NC surface or its environment.

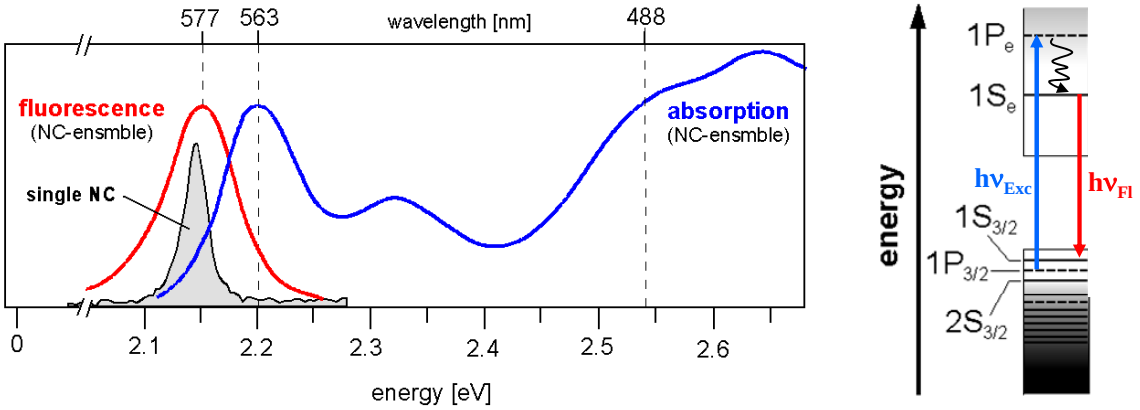

Figure 10: (Left) Comparison of the room temperature optical absorption and photoluminescence spectra of a CdSe NC ensemble with narrow size distribution, as well as the luminescence of individual NC. (Right) Energy levels involved in the optical absorption and fluorescence of a CdSe NC.

Individual NC emission spectra acquired at cryogenic temperatures exhibit a very narrow linewidth of a few nm or less, with distinguishable longitudinal-optical (LO) phonon side-lines. There is also a broad and less intense luminescence maximum at 300 - 700 meV below the excitation energy, arising from electron or hole transition into the surface states in the NC. The surface state emission intensity is very sensitive to the removal and the exchange of the ligand layer. Conversely, efficient room temperature band edge emission is only observed for NCs with proper surface passivation because otherwise charge carriers are very likely to be trapped in surface states, thereby enhancing non-radiative recombination. Good surface passivation can be achieved by changing the nature of the organic ligands after the NC synthesis. Appropriate ligands for substituting the TOPO cap on CdSe NCs include alkyl amines, which are capable of increasing the fluorescence quantum efficiency from about 10% to values of 40 - 50% [9].

2.3 Core-shell quantum dots

Surface engineering is an important tool to control the properties of the NCs and in particular the optical ones. One important strategy is the above described attachment of stabilizing organic ligands to the NC surface. However, in view of further NC functionalization, it is highly desirable to provide a surface passivation which is insensitive to subsequent ligand exchange. A suitable and widely applied method consists of the growth of a lattice-matched, higher band gap inorganic shell on the NC surface, which results in core-shell (CS) systems [10] (figure 11). The shell layer serves a double purpose: it eliminates core surface traps and it confines the excitation into the core. CdS (E_g = 2.5 eV) and ZnS (E_g = 3.8 eV) have mainly been used as shells for CdSe cores (E_g = 1.8 eV at 300 K). While CdS is better lattice-matched to CdSe, ZnS has a larger band offset and better confinement. Growing an optimized shell on top of the core dramatically

increases the quantum yield, up to values of ~80%, although more typical values fall around 20 - 50%. The shell furthermore protects surface atoms of the core from oxidation and other chemical reactions, and thus enhances the photo-stability by several orders of magnitude relative to conventional dyes. In general, particles passivated with inorganic shell structures are more robust than organically passivated dots and have greater tolerance to processing conditions necessary for incorporation into solid state structures.

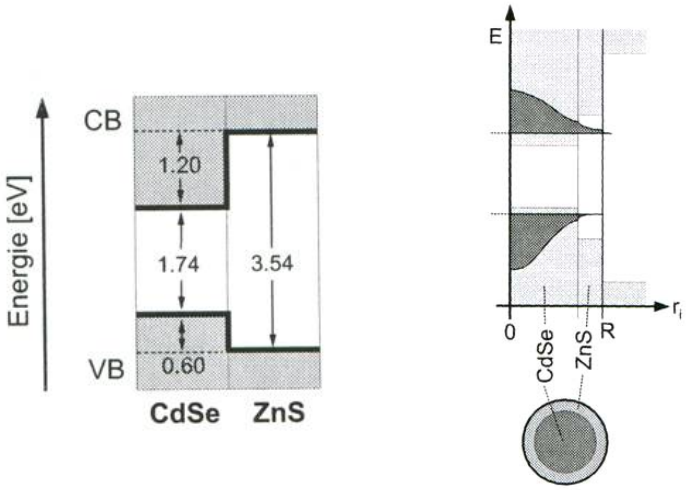

Figure 11: Scheme of the band alignment within a CdSe/ZnS core-shell nanocrystal, and the resulting confinement of the wavefunction in the CdSe core.

A general requirement for the synthesis of CS NCs with satisfactory optical properties is epitaxial-type shell growth. The control of the shell thickness is a delicate point which deserves special attention. If the shell is too thin, the passivation of the core NCs is inefficient resulting in reduced photo-stability. In the opposite case, the optical properties of the resulting CS NCs deteriorate as, driven by the lattice mismatch of the core and shell materials, defects are created with increasing shell thickness. CS systems are generally fabricated in a two-step procedure, consisting of core NCs. synthesis, followed by a purification step, and the subsequent shell growth reaction, during which a small number of monolayers (typically 1 to 5) of the shell material are deposited on the cores. An advanced approach for shell growth derived from chemical bath deposition techniques and aiming at the precise control of the shell thickness is the so-called SILAR (successive ion layer adsorption and reaction) method. It is based on the formation of one monolayer at a time by alternating the injections of cationic and anionic precursors and has firstly been applied for the synthesis of CdSe/CdS CS systems. In this manner, monodispersity of the samples can be maintained for CdS shell thicknesses up to five monolayers.

2.4 Nanocrystal superstructures

Ordered arrays or superstructures of semiconductor NCs with narrow size distribution have been obtained through a variety of methods. Packing the NCs into a dense array can have a noticeable effect on their optical properties. For instance, the emission spectra of CdSe NC superstructures display a red-shift in comparison to a dilute solution of the

same particles, indicative of some extent of inter-dot coupling [11]. The observed shift has been associated with long-range resonant energy transfer from the smaller to the larger dots within the sample.
In the superstructures investigated so far, the coupling between the QDs is purely dipole-type, *i.e.*, true quantum coupling (exchange coupling via quantum mechanical wavefunction overlap) has yet to be observed. This task would require to prepare arrays such that the dipoles of all the individual particles are in crystallographic alignment with one another, and to reduce the interparticle separation distance to just a couple of Angstroms (usually the organic passivating ligands at the nanocrystal restrict the approach between the semiconductor cores).

2.4.1 One-dimensional NC superstructures

Semiconductor NCs with large dipole moments can form chains in a colloidal solution due to strong dipole–dipole interactions. Chaining of NCs has for instance been observed in colloidal solutions of PbSe NCs (figure 12). In the chains, the NCs can fuse together by the mechanism of oriented attachment along identical crystal faces forming single-crystalline nanowires [12].

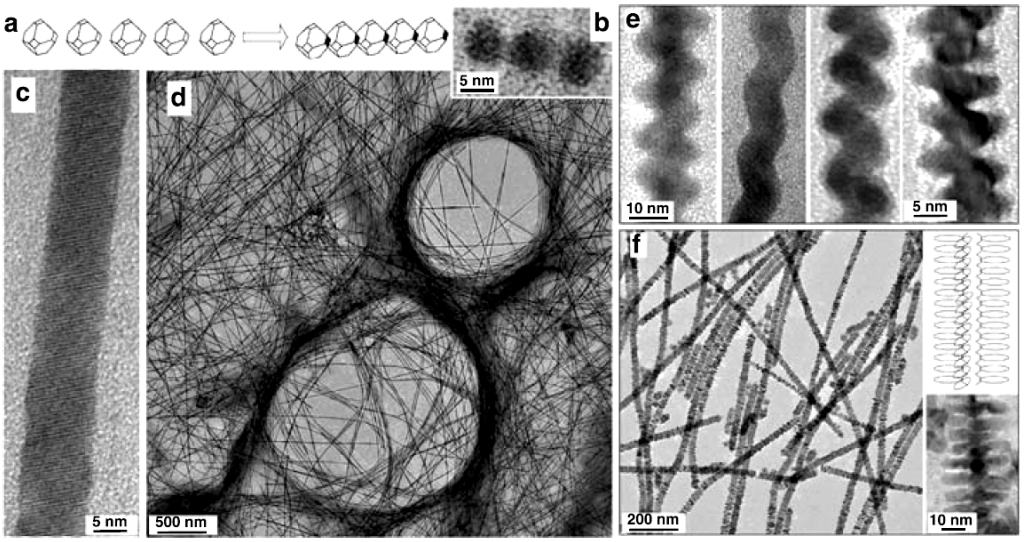

Figure 12: PbSe nanowires synthesized by 1D assembly and oriented attachment of NC building blocks. a) Schematic representation of the oriented attachment process. b) HRTEM image of a "trimer" formed at the early reaction stage. c) High-resolution and d) overview TEM images of straight PbSe nanowires. e) TEM images of zig-zag and helical PbSe nanowires. f) TEM images and a corresponding scheme of branched PbSe nanowires.

In NCs with wurtzite structure (*e.g.*, CdSe), a significant electric dipole moment originates from the non-centrosymmetric atomic lattice and scales with the nanoparticle volume. By contrast, the origin of dipoles in PbSe NCs, which have centrosymmetric atomic unit cell, can be explained by asymmetric lattice truncations or non-centrosymmetric arrangement of Pb- and Se-terminated {111} facets. Indeed, high-resolution TEM analysis has confirmed that PbSe nanocrystals are terminated by six

{100} and eight {111} facets. The {100} facets are formed by both Pb and Se atoms, while the {111} facets must be either Se- or Pb-terminated. Due to the difference in electronegativities between Pb and Se, {111} facets are polar and their arrangement will determine the distribution of electric charge within the PbSe NC. Depending on the mutual arrangement of the ⟨111⟩ facets, the whole NC can either have central symmetry and thus a zero net dipole moment or it can lack central symmetry and possess a dipole moment along the ⟨100⟩, ⟨110⟩, or ⟨111⟩ axes, respectively. Assuming a random distribution of polar ⟨111⟩ facets and cuboctahedral shape PbSe, the majority of PbSe NCs (~89%) is expected to have non-zero dipole moments which drive their oriented attachment.
The 1D assembly and oriented attachment of NC building blocks yields large quantities of high quality, catalyst-free semiconductor nanowires. In addition to straight nanowires, zig-zag, helical, branched, and tapered nanowires as well as single-crystal nanorings have been prepared by the adjustment of the reaction conditions.

2.4.2 Two-dimensional NC superstructures

Two-dimensional self-assembly of semiconductor NCs can occur both on solid substrates and liquid surfaces. Simple solvent evaporation often leads to the formation of more sophisticated patterns (figure 13), such as NC densely packed monolayers, rings, or dendrites.

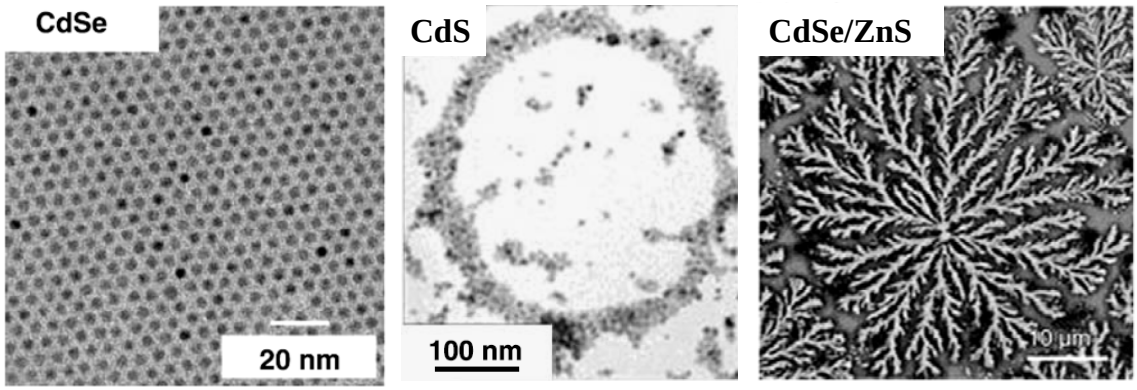

Figure 13: TEM images of different types of semiconductor NCs assembled into a dense monolayer (left), a nanoring (middle), and a dendrite superstructure.

One possible mechanism of NC ring formation involves nucleation and growth of holes in the solvent films completely wetting the substrate. Hole nucleation in an evaporating film can be modeled as substrate-mediated boiling, and hole formation can be considered as bubble nucleation in a bulk of superheated liquid with the only difference that holes in thin films are “open” to the vapor above the film [13]. The growth of holes pushes the particles and solvent out toward the “bulk” wet film of colloidal solution. If the nucleation and growth of holes are separated in time, rings uniform in width will be formed. The force acting on the hole rim increases linearly with the size of the hole, and the number of particles being swept out by the hole area increases quadratically. The concentration of nanoparticles inside the ring is significantly lower as compared to

particle concentration outside. In this model the particle-particle attractions are considered not to exceed thermal energies. As a result, NCs can be moved until the friction arising from their attraction to the substrate pin the contact line. The resulting hole size depends on particle size and their concentration. In the case of low concentrations, the contact lines of the holes will not be pinned before the "percolation" of the growing holes and compact domains of nanoparticles will be formed. The smaller size of nanoparticles also favors the growth of compact nanoparticle domains, *i.e.*, small particles can more easily overcome their static friction and as a result, the pinning size of hole becomes larger than the average distance between holes.

Ring-like NC patterns can also result from the Marangoni effect. Evaporation of a thin film of volatile solvent can create significant temperature variation between the substrate and the free upper surface leading to the temperature gradient across the film. The interfacial tension depends on the temperature and, as a result, local "hot" and "cold" spots generate low and high interfacial areas pulling the solvent from the warmer to cooler areas. At the same time solvent moves upward to the warmer places in order to compensate the concentration perturbation. This generates a convective flow through the liquid film and leads to the appearance of a network of cells. Inside those the fluid goes up by the center of the cells and goes down by the walls of the cells. The dimensionless parameter determining the threshold of this dynamic solvent instability is called the Marangoni number M_a:

$$M_a = -\frac{d\sigma}{dT}\frac{1}{\eta\alpha}L\Delta T$$

where σ is the surface tension (N/m), η is the dynamic viscosity (kg/(ms)), α is the thermal diffusivity (m^2/s), L is the film thickness, and ΔT is the temperature difference. The critical value for the Marangoni number is M_a = 80. Below this value interfacial instabilities do not appear, whereas above 80 different patterns can be generated, depending on the system [14]. Increase in temperature and interfacial tension fluctuations, as well as in the thickness of the liquid film promote the appearance of interfacial instabilities, while fluctuation enhancement is suppressed by thermal diffusivity and dynamic viscosity of the liquid.

Dendrites are another interesting example of self-assembled 2D NC superstructures. They are formed as a result of the interplay between the ordering effect of crystallization, the disordering effect of local orientation fluctuations of the nanoparticles, and the freezing of the domain edges after complete solvent evaporation. Typically, dendrites formed from nearly spherical NCs consist of a core with six-to-ten branches. Increase of the NC concentration as well as evaporation temperature was found to cause gradual decrease of the lateral sizes of dendrites and an increase of their thickness.

2.4.3 Three-dimensional NC superstructures

Semiconductor NCs can also form 3D superstructures with different degrees of short- and long-range ordering. Individual NCs can be brought together as freestanding structures or thin films in two forms: (i) amorphous (glassy) and (ii) crystalline solids. Glassy solids

are isotropic materials with only short-range order and randomly oriented nanoparticles. Close-packed glassy films usually form if the nanoparticles are polydisperse or if the rate of destabilization of a colloidal solution is high (*e.g.*, very fast solvent evaporation). Compared to glassy films, periodic NC superstructures are more attractive for practical applications and fundamental studies of their properties. Generally, both entropy and isotropic attractive van-der-Waals forces are expected to favor the assembly of spherical particles into the structures with highest packing density such as face-centered cubic (fcc) and hexagonally close-packed (hcp) lattices. In fcc and hcp lattices, subsequent hexagonally close-packed layers are shifted with respect to each other in a way that centers of mass in one layer are above the hole in the layer below. This results in three different layer positions denoted as A, B and C. The fcc and hcp lattices exhibit a respective ABCABC- and ABAB-type stacking of hexagonally packed layers.

In an ensemble of non-interacting hard spheres entropy can be a sole driving force for the transition from disordered into long-range ordered state. This transition spontaneously occurs when the volume fraction of monodisperse hard spheres exceeds a threshold value of 0.494. Theoretical simulations of hard-sphere colloidal crystals predict the fcc structure to be slightly more stable compared to hcp, on the order of $\sim 10^{-3}$ $k_B T$ per particle [15]. In agreement with this prediction, monodisperse micron-size latex and silica spheres, whose behavior is similar to hard spheres, exhibit predominantly fcc superlattices, also known as synthetic opals, whereas the hcp phase does not form. Kinetic factors associated with solvent flow can also play an important role in determining structure of nanoparticle superlattices, usually favoring the formation of fcc phase.

Both fcc and hcp structures have been found in CdSe NC 3D superstructures. In real NC superlattices, the effects associated with the slight deviation of NC shape from spherical, the presence of dipole moments, or coupling of higher order multipole moments can noticeably influence the relative stabilities of fcc and hcp phases. Dipolar coupling of NCs in a superlattice normally imparts a higher stability to the hcp structure, due to more favorable dipolar coupling.

3. 1D-nanostructures: Semiconductor nanowires (NWs)

3.1 VLS growth of semiconductor NWs

Semiconductor NWs are generally synthesized by employing metal nanoclusters as catalyst via a vapor-liquid-solid (VLS) process, as exemplified in figure 14 for the synthesis of Si-NWs. In this process, the metal nanoclusters are heated above the eutectic temperature for the metal-semiconductor system of choice in the presence of a vapor-phase source of the semiconductor, resulting in a liquid droplet of the metal/semiconductor alloy. The continued feeding of the semiconductor reactant into the liquid droplet supersaturates the eutectic, leading to nucleation of the solid semiconductor. The solid-liquid interface forms the growth interface, which acts as a sink causing the continued semiconductor incorporation into the lattice and, thereby, the growth of the nanowire with the alloy droplet riding on the top. The gaseous semiconductor reactants can be generated through decomposition of precursors in a chemical vapor deposition (CVD) process or through momentum and energy transfer

methods such as pulsed laser ablation or molecular beam epitaxy (MBE) from solid targets. So far, CVD has been the most popular technique.

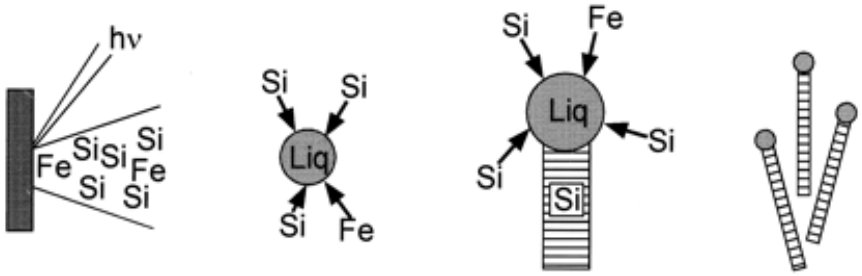

Figure 14: Synthesis of silicon nanowires via the vapor-liquid-solid (VLS) mechanism (four subsequent stages are displayed from left to right), exemplified for Si nanowires grown from iron nanoparticles. In the present case, the required Si vapor is generated by laser ablation.

The VLS process has become a widely used method for producing NWs from a rich variety of materials, including elemental semiconductors (Si, Ge, and B), III-V semiconductors (Ga N, GaAs, InP, InAs), and II-VI semiconductors (ZnS, CdS, CdSe). The obtained nanowires are remarkable for their uniform diameters, which can be controlled by the size of the used metal catalyst particles. VLS growth has been employed in the synthesis of Si nanowires with diameters approaching molecular dimensions (using monodisperse Au nanocrystals as catalyst, and SiH_4 as vapor-phase reactant), or CdS nanowires with diameter down to a few nm. In the latter case, an organic cadmium compound [$Cd(S_2CNEt_2)_2$] has been utilized as single-source molecular precursor [16]. This compound is thermally decomposed in the growth region of a furnace, forms a liquid Cd-S-Au solution with the Au nanoparticle catalysts, and then undergoes nucleation and nanowire growth.

The diameter of the obtained NWs is determined by that of the starting nanocluster, and uniform, atomic-scale NWs can be obtained in a well-controlled growth process as nanoclusters with diameters down to a few nanometers are now commercially available. There are two competing interfaces during nanowire growth, the liquid/solid interface between the eutectic and the nanowire and the gas/solid interface between the reactants and the exposed surface of the growing nanowire. Precipitation through the first interface results in the VLS growth and axial elongation of the nanowire, while dissociative adsorption on the second interface results in vapor-solid growth and thickening in the radial direction. Either mechanism can be dominating in an actual growth process, depending on the detailed growth condition such as the pressure, flow rate, temperature, reactant species and background gases that are by-products of growth reactions. For example, in the Si-NW growth process, low temperature growth can reduce the rate of direct thermal dissociation of silane; hence, axial nanowire growth is favored. Hydrogen has also been found to mitigate radial growth through suppression of either the adsorption of the reactants by terminating the Si surface or of the dissociation of silane. The use of H_2 as the carrier gas also passivates the NW surface in a manner similar to that observed in thin-film growth and reduces roughening along the NW. Uniform NWs with negligible diameter variation can thus be achieved through careful control of the growth conditions,

including the employment of local heaters to reduce uncontrolled decomposition of silane. On the other hand, tapered NWs are products from simultaneous growth in both the axial and radial directions and are generally not desirable for most electrical and optical applications.

3.2 Electronic structure of semiconductor NWs

If we take the confining potential of a semiconductor material related to spatial position **r** = (y, z), the electrons remain free to move along x and the result is a wire, closely analogous to an electromagnetic wave guide. Starting with the 2D Schrödinger equation for the confining potential (assumed to be zero inside and infinitely high outside of the NW):

$$\left[-\frac{\hbar^2}{2m^*}\left(\frac{\partial^2}{\partial x^2}+\frac{\partial^2}{\partial y^2}\right)+V(r)\right]\psi_{n,m}(r)=E_{n,m}\,\psi_{n,m}(r)$$

the wavefunction solutions for a nanowire with rectangular cross-section (height *a* and width *b*) are obtained as

$$\psi_{n,m}(x,y,z)=\left(\frac{4}{ab}\right)^{1/2}\sin\frac{n\pi y}{a}\,\sin\frac{m\pi z}{b}\,e^{ikx}$$

where *m*, *n* = 1, 2, 3,... The free electron-like motion along the wire leads to subbands of states with energies

$$E_{n,m}(k_x)=\frac{n^2\pi^2\hbar^2}{2m^*a^2}+\frac{m^2\pi^2\hbar^2}{2m^*b^2}+\frac{\hbar^2k_x^2}{2m^*}$$

3.3 Optical properties of semiconductor nanowires

Photoluminescence (PL) spectra obtained from nanowires of varying diameters indicate that the emission maxima systematically shift to higher energy with decreasing nanowire diameter. As an example, InP nanowires should exhibit size-dependent PL for diameters less than the bulk exciton diameter (~19 nm). Experimentally, a systematic shift to higher energy could be observed for InP nanowire diameters below 20 nm, in close agreement with the expected radial quantum confinement.

Another important property of semiconductor nanowires is the polarization anisotropy of their interband transitions: due to the 1D confinement, the emission/absorption intensity $I_{//}$ for light polarized parallel to the wire axis (*z*) can be different from that ($I_{\perp}$) for light polarized in the (*x,y*) plane, perpendicular to it. The polarization anisotropy is defined in terms of the degree of linear polarization

$$\rho = \frac{\alpha_{||} - \alpha_{\perp}}{\alpha_{||} + \alpha \perp}$$

where α is the absorption coefficient. Furthermore, as the underlying crystal structure of the wire might be different along two perpendicular directions in the (*x,y*) plane, an in-plane polarization anisotropy can also be expected. A giant anisotropy in the band gap emission, which was found to be over 90% polarized parallel to the wire axis, was measured in cylindrical InP nanowires (figure 15) [17].

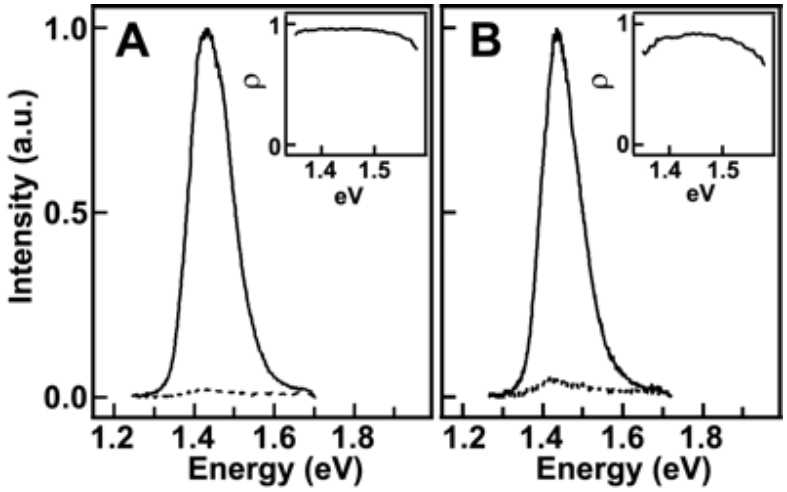

Figure 15: Polarized excitation (*panel A*) and luminescence (*panel B*) spectra of an individual InP nanowire 15 nm in diameter, recorded at room temperature (the full and broken lines correspond to polarization of the electric field vector parallel and perpendicular to the wire long axis, respectively. In both cases, the polarization ratio ρ reaches values close to 1.0.

3.4 Device applications of semiconductor nanowires

The strongly polarized optical absorption of semiconductor NWs makes them attractive for photodetection devices. Electronic conductivity in semiconductor nanowires is substantially enhanced by exposing these structures to photons of energy greater than their band-gaps. Polarization-sensitive photodetectors have been demonstrated from individual InP nanowires [17]. Upon light illumination (λ_{exc} = 514.5nm), the wire conductance increases by two to three orders of magnitude with increasing excitation power density. The photocurrent response of the InP wires shows a pronounced polarization anisotropy, with the conductance for parallel excitation being more than an order of magnitude larger than for perpendicular excitation. The photoconductivity anisotropy ratio, $\sigma = (G_{//} - G_{\perp})/(G_{//} + G_{\perp})$, where $G_{//}$ ($G_{\perp}$) is the conductance with parallel (perpendicular) excitation, is close to 1.0, in excellent agreement with the polarization ratio measured from PL. In addition, the photocurrent oscillation observed upon continuously rotating the excitation polarization vector clearly proofs the high reproducibility of the PC polarization response (figure 16).

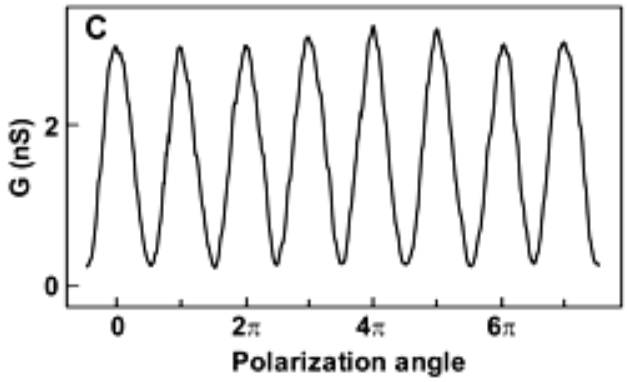

Figure 16: Room temperature conductance of an individual InP nanowire (20 nm diameter) in dependence of the polarization angle of the incoming polarized light with a wavelength of 514.5 nm (0° corresponds to parallel orientation between the electrical field vector and the long axis of the wire).

Further perspectives are opened by integrating a larger number of nanowires into an electrical device. As the simplest realization, crossed-nanowire devices composed of one n-type doped (by Te) and one p-type doped (by Zn) InP nanowire have been studied [18]. I-V traces of the p-n junctions created in this manner are highly rectifying, in contrast to the individual nanowires which display linear (ohmic) characteristics. Similarly, linear behavior is observed for n-n (and p-p) nanowire junctions, proving the absence of an oxide or contamination layer between the wires, which would produce a significant tunneling barrier. The diode-like behavior of the crossed-wire p-n junctions is similar to bulk semiconductor p-n junctions, which form the basis for numerous critical electronic and optoelectronic devices.

3.5 Nanowire heterostructures

The VLS process provides convenient access to 1D heterostructures in a controlled fashion. Both axial heterostructures, in which sections of different materials with the same diameter are grown along the wire axis, and radial heterostructures, in which core/shell and core/multi-shell form along the radial direction, have been realized for VLS-CVD grown NWs. The formation of NW heterostructures within the VLS method can be understood by considering the possible effects of a change in reactant vapor once nanowire growth has been established. If vapor decomposition/adsorption continues exclusively at the surface of the catalyst nanocluster site, crystalline growth of the new semiconductor will continue along the axial direction. On the other hand, if the decomposition of the new vapor/reactant on the surface of the semiconductor nanowire cannot be neglected, a shell of material will grow on the original nanowire surface. Repeated changing of reactants in a regime favoring axial growth will lead to the formation of a nanowire superlattice, while changing reactants in a radial-growth regime will result in core-multi-shell radial structures. In principle, any material suitable for planar film deposition can be deposited on the surface of a nanowire, and crystalline radial heteroepitaxy only requires that the nanowire surface is crystalline.

3.5.1 Axial nanowire heterostructures

Axial nanowire heterostructures can be obtained by alternative introduction of vapor phase reactants that react with the same nanocluster catalyst. A critical requirement of the axial nanowire heterostructure growth is that a single nanocluster catalyst can be found which is suitable for growth of the different components under similar conditions. For a wide range of III-V and IV materials, Au nanoclusters can meet this requirement. Using Au nanoclusters as catalysts and a laser-assisted catalytic growth, GaAs/GaP axial nanowire heterostructures have been successfully obtained with GaAs and GaP targets at temperatures of 700-850°C in a continuous argon flow. By repeating the modulation process, nanowire superlattices can be produced in which the number of periods and repeat spacing can be readily varied during growth. GaAs/GaP superlattices obtained in this manner are of interest for photonic applications, because GaAs is a direct bandgap semiconductor, while GaP has an indirect gap. PL images of individual $(GaP/GaAs)_3$ nanowires exhibit an emission pattern of three spots separated by dark regions [19]. This pattern is consistent with emission originating from the three GaAs regions, separated by dark GaP regions that act as optical 'spacers'. The GaAs regions exhibit a strong polarization dependence, with maximal emission observed when the excitation is polarized parallel to the nanowire axis. Likewise, the PL emission is highly polarized along the wire axis.
As a tool for analyzing the abruptness of the interfaces in simple two-phase systems, HRTEM has proven to be superior to alternative methods such as energy dispersive spectroscopic imaging (EDS) and energy filtered TEM imaging (EFTEM), as has been demonstrated for InAs/InP nano-whiskers [20]. The sharp InAs-InP interfaces impose a steeplechase-like potential structure on the whiskers with an expected band offset in the conduction band of 0.6 eV. This energy landscape strongly affects the electrical transport behavior (figure 16).

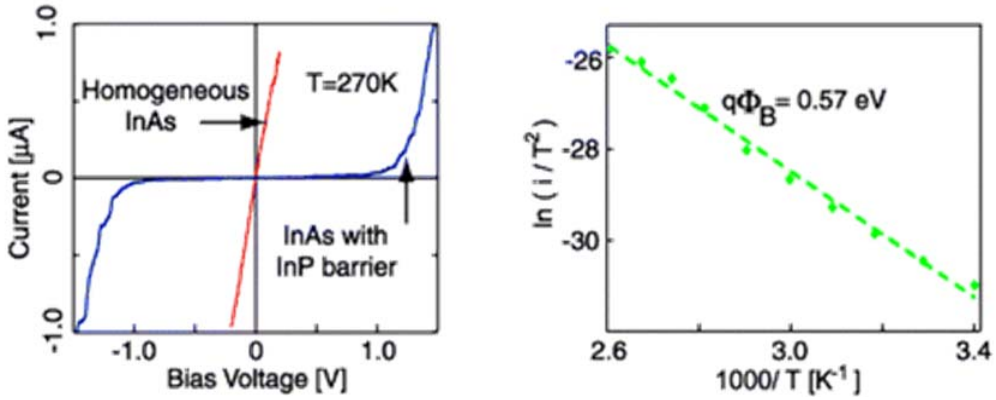

Figure 16: I-V characteristic of a homogeneous InAs nanowhisker compared to that of a InAs nanowhisker containing an InP barrier at 270 K (*left*). From the temperature dependence of the current through the InAs/InP heterostructure, a barrier height of 0.57 eV is extracted, in very good agreement with the expected conductance band offset (*right*).

The I-V characteristic of the InAs/InP heterostructure is strongly nonlinear, with a voltage bias of more than 1 V required to induce a measurable current, in marked contrast to pure InAs whiskers which exhibit linear behavior and considerably lower resistance. The nonlinear characteristic is associated with thermal excitation of carriers over the internal InP barrier. Temperature dependent measurements yield an effective barrier height of ~0.6 eV, in very good agreement with the expected value for the conduction band offset.

3.5.2 Radial nanowire heterostructures

Radial core/shell heterostructures can be achieved if dissociation of the reactants is promoted at the grown NW surface, analogous to the layered growth of planar heterostructures. Compared with NWs in the simple homogeneous form, core/shell heterostructure NWs offer better electrical and optical properties as they can now be tailored through band structure engineering. One example is the CVD synthesis of epitaxial Ge-Si core-sheath wires [21]. In this approach, homogeneous deposition on the core Ge nanowire (grown through gold particle-directed axial growth) has been favored through the addition of diborane (B_2H_6), which serves to lower the decomposition temperature of the silicon precursor (SiH_4). Lattice-resolved high-resolution TEM analysis of the Ge-Si core-shell nanowires reveals the presence of crystalline Ge cores and predominantly amorphous Si shells, with a Ge-Si interface width below 1 nm. The amorphous Si shell can be completely crystallized via subsequent thermal annealing at 600°C, which leaves the abrupt Ge-Si interface largely unaffected. By comparison, Si-Ge core-shell wires with a fully crystallized Ge-shell and a sharp (< 1 nm) Si-Ge interface can be directly obtained via a low-temperature growth process. This difference is most probably due to the higher surface mobility of the Ge adatoms.

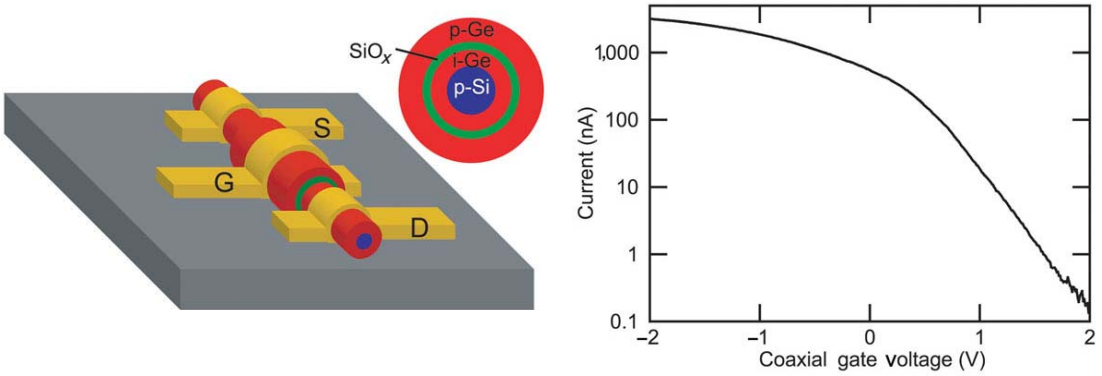

Figure 17: (Left) Schematic depiction of a field-effect transistor made from a p-Si/i-Ge/SiO_x/p-Ge core-multishell structure. (Right) Transistor current measured at room temperature as a function of coaxial gate voltage.

Furthermore, the coaxial geometry of these nanostructures offers the possibility to fabricate novel devices like coaxially gated nanowire field-effect transistors (FETs). A first prototype has been realized from a p-Si/i-Ge/SiO_x/p-Ge core-multishell structure, in which the i-Ge shell constitutes the active channel, as illustrated by figure 17. To fabricate the FET, the source, drain and gate contacts were made by selective etching and

metal deposition onto the inner i-Ge shell and outer p-Ge shell, respectively. The obtained FETs show high transconductance values of up to 1500 nAV^{-1} at a source-drain bias of 1 V [21], which competes favorably with FETs based upon CMOS technology.

References:

[1]: V.K. LaMer, R.H. Dinegar, J. Am. Chem. Soc. 72 (1950), 4847.

[2]: T. Sugimoto, Adv. Colloid Interface Sci. 28 (1987), 65.

[3]: C.B. Murray, D.J. Norris, M.G. Bawendi, J. Am. Chem. Soc. 115 (1993), 8706.

[4]: Y. Yin, A.P. Alivisatos, Nature 437 (2005), 664.

[5]: P.S. Nair, K.P. Fritz, G.D. Scholes, Chem. Commun. (2004), 2084.

[6]: L. Manna, D.J. Milliron, A. Meisel, E.C. Scher, A.P. Alivisatos, Nature Materials 2 (2003), 382.

[7]: D.J. Norris, A.L. Efros, M. Rosen, M.G. Bawendi, Phys. Rev. B 53 (1996), 16347.

[8]: D.J. Norris, A. Sacra, C.B. Murray, M.G. Bawendi, Phys. Rev. Lett. 72 (1994), 2612.

[9]: D.V. Talapin, A.L. Rogach, A. Kornowski, M. Haase, H. Weller, Nano Letters 1 (2001), 207

[10]: A. Mews, A. Eychmüller, M. Giersig, D. Schoos, H. Weller, J. Phys. Chem. 98 (1994), 941.

[11]: C.R. Kagan, C.B. Murray, M.G. Bawendi, Phys. Rev. B 54 (1996), 8633.

[12]: Z. Tang, N.A. Kotov, M. Giersig, Science 297 (2002), 237.

[13]: P.C. Ohara, J.R. Heath, W.M. Gelbart, Angew. Chem. Int. Ed. 15 (1997), 1078.

[14]: T. Ondarcuhu, J. Millan-Rodriguez, H.L. Mancini, A. Garcimartin, C. Perez-Garcia, Phys. Rev. E 48 (1993), 1051.

[15]: P.G. Bolhuis, D. Frenkel, S.C. Mau, D.A. Huse, Nature 388 (1997), 235.ö

[16]: C.J. Barrelet, Y. Wu, D.C. Bell, C.M. Lieber, J. Am. Chem. Soc. 125 (2003), 11498.

[17]: J.F. Wang, M.S. Gudiksen, X.F. Duan, Y. Cui, C.M. Lieber, Science 293 (2001), 1455.
[18]: X.F. Duan, Y. Huang, Y. Cui, J.F. Wang, C.M. Lieber, Nature 409 (2001), 66.

[19]: M.S. Gudiksen, L.J. Lauhon, J. Wang, D.C. Smith, C.M. Lieber, Nature 415 (2002), 617.

[20]: M.T. Björk, B.J. Ohlsson, T. Sass, A.I. Persson, C. Thelander, M.H. Magnusson, K. Deppert, L. Samuelson, Nano Letters 2 (2002), 87.

[21]: L.J. Lauhon, M.S. Gudiksen, C.L. Wang, C.M. Lieber, Nature 420 (2002), 57.

General review articles:

- T. Trindade, P. O'Brien, N.L. Pickett, "Nanocrystalline Semiconductors: Synthesis, Properties, and Perspectives", Chem. Mater. 13 (2001), 3843.

- M.G. Bawendi, M.L. Steigerwald, L.E. Brus, "The quantum mechanics of larger semiconductor quantum dots", Ann. Rev. Phys. Chem. 41 (1990), 477.

- M.A. El-Sayed, "Small is different; Shape-, size- and composition-dependent properties of some colloidal semiconductor nanocrystals", Acc. Chem. Res. 37 (2004), 326.

- A.D. Yoffe, "Semiconductor quantum dots and related systems: electronic, optical, luminescence and related properties of low dimensional systems", Adv. Phys. 50 (2001), 1.

- C.B. Murray, C.R. Kagan, M.G. Bawendi, "Synthesis and characterization of monodisperse nanocrystals and close-packed nanocrystal assemblies", Ann. Rev. Mater. Sci. 30 (2000), 545.

- R. Agarwal, C.M. Lieber, "Semiconductor nanowires: optics and optoelectronics", Appl. Phys. A 85 (2006), 209.

- G.Z. Shen, D. Chen, Y. Bando, D. Goldberg, "One-dimensional (1-D) nanoscale heterostructures", J. Mater. Sci. Technol. 24 (2008), 541.

- Y. Ding and Z.L. Wang, "Structure analysis of nanowires and nanobelts by transmission electron microscopy", J. Phys. Chem. B 108 (2004), 12280.